ACS **APPLIED** MATERIALS & INTERFACES

Research Article

Enhanced Photocatalytic and Antibacterial Ability of Cu-Doped Anatase TiO$_2$ Thin Films: Theory and Experiment

Abdullah M. Alotaibi, Benjamin A. D. Williamson, Sanjayan Sathasivam, Andreas Kafizas, Mahdi Alqahtani, Carlos Sotelo-Vazquez, John Buckeridge, Jiang Wu, Sean P. Nair, David O. Scanlon,* and Ivan P. Parkin*

Read Online

ACCESS | Metrics & More | Article Recommendations | SI Supporting Information

ABSTRACT: Multifunctional thin films which can display both photocatalytic and antibacterial activity are of great interest industrially. Here, for the first time, we have used aerosol-assisted chemical vapor deposition to deposit highly photoactive thin films of Cu-doped anatase TiO$_2$ on glass substrates. The films displayed much enhanced photocatalytic activity relative to pure anatase and showed excellent antibacterial (vs *Staphylococcus aureus* and *Escherichia coli*) ability. Using a combination of transient absorption spectroscopy, photoluminescence measurements, and hybrid density functional theory calculations, we have gained nanoscopic insights into the improved properties of the Cu-doped TiO$_2$ films. Our analysis has highlighted that the interactions between substitutional and interstitial Cu in the anatase lattice can explain the extended exciton lifetimes observed in the doped samples and the enhanced UV photoactivities observed.

KEYWORDS: *photocatalysis, antibacterial, thin films, TiO$_2$, CVD, hybrid-DFT*
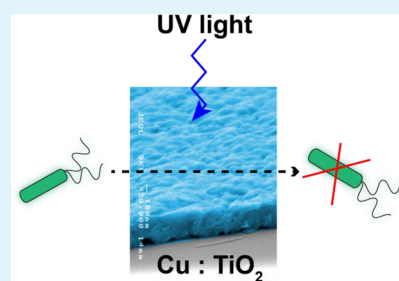
INTRODUCTION

Anatase TiO$_2$ is the leading chemically and biologically stable, inexpensive semiconductor with photosensitive properties for applications in photocatalysis and antibacterial surfaces.[1−9] For both applications, the general mechanisms for the functional properties are very similar;[3,10] when TiO$_2$ is irradiated with photons with energy greater than or equal to the band gap energy, electrons from the valence band are promoted to the conduction band and concomitant holes are formed in the valence band. These electrons and holes can migrate to the surface of the semiconductor and react with water and oxygen to produce reactive oxygen species (ROS).[10,11] These ROS can oxidize a wide range of organic species, including pollutants, bacteria, cancer cells, and viruses. In the case of bacteria, the ROS produced cause an oxidative stress on bacterial cells that destroy cell walls, DNA, and proteins.[10] This form of antibacterial activity and decontamination of surfaces is innovative as it provides effective relief against bacteria that have grown resistant to many conventional antimicrobial agents, in part due to decades of inappropriate antibiotic use.[12,13] Applying such coatings on high contact touch surfaces such as door handles and keyboards in hospital and health care environments has shown a marked reduction of health care-associated infections.[14]

ROS are destructive not only to bacteria but also to organic pollutants that can be found in air and water. In fact, the primary application of TiO$_2$ as a photocatalyst is as a self-cleaning transparent coating on windows to assist in the breakdown of dirt.[1] The incorporation of dopant quantities of

Cu into the TiO$_2$ matrix has dual advantages. Not only can Cu be used as an antibacterial agent by itself, through Fenton-type reactions, but TiO$_2$:Cu can also potentially reduce the recombination of charge carriers which are important for both antibacterial and self-cleaning applications of TiO$_2$.[15−19]

Cu-doped TiO$_2$ has been prepared via solution[17−22] and nonsolution[23]-based routes in nanoparticulate forms mainly for photocatalytic and ferromagnetic applications. Sol−gel techniques[24] and physical vapor deposition methods such as magnetron sputtering[25] have also been used to fabricate thin films.

In this paper, we demonstrate for the first time the synthesis of Cu-doped TiO$_2$ films using an aerosol-assisted chemical vapor deposition (AACVD) method. AACVD is a facile technique that places only the limitation of solubility on the precursors, that is, there are no volatility concerns as with traditional CVD, thus allowing a wider range of precursors to be employed.[26−31] It is also an atmospheric pressure technique that has been used to grow a wide range of films for various applications with the potential for upscale.[32−35]

Both pure and Cu-doped TiO_2 films were prepared via AACVD, and their photocatalytic activity to the degradation of a model organic pollutant, stearic acid, and antibacterial activity to bacteria *Escherichia coli* and *Staphylococcus aureus* was examined under 365 nm radiation and compared. Cu-doped TiO_2 films showed enhanced photocatalytic [formal quantum efficiency (FQE) of 1.1×10^{-4} molecules photon^{-1} for 5% Cu-doped TiO_2] and antimicrobial activities (destruction of *E. coli* and *S. aureus* to almost undetectable levels under 4 h of 365 nm irradiation) compared with pure TiO_2. Transient absorption spectroscopy (TAS) studies showed that photogenerated charge carriers were longer-lived in Cu-doped TiO_2 films. Hybrid functional ab initio density functional theory (DFT) calculations were also carried out in order to determine the mechanism for the enhancement in photocatalytic activities and charge carrier lifetimes that Cu-doped anatase provides.

■ EXPERIMENTAL METHODOLOGY

All chemicals used were purchased from Sigma-Aldrich Chemical Co. and used as received. Deposition was carried out on an $150 \times 45 \times 4.5$ mm SiO_2 (50 nm)-coated float glass (SiO_2 acts as a barrier layer preventing the diffusion of ions from within the glass into the deposited film) which has been supplied by Pilkington NSG. Prior to use, the glass substrates were thoroughly cleaned using acetone (99%), isopropanol (99.9%), and distilled water and dried in air.

Deposition Procedure. Deposition was carried out under N_2 (BOC Ltd., 99.99% purity) flow using titanium isopropoxide $[Ti(OCH(CH_3)_2)_4]$ (99%), copper nitrate (hydrated), $[Cu(NO_3)_2 \cdot 3H_2O]$ (99%), and ethyl acetate (99%).

$[Ti(OCH(CH_3)_2)_4]$ (0.5 g, 1.76 mmol) was dissolved in ethyl acetate (30 mL) in a glass bubbler. The resulting solution was atomized using a piezoelectric device (Johnson Matthey Liquifog). For the Cu-doped TiO_2 films, $[Cu(NO_3)_2 \cdot 3H_2O]$ (2, 5, 10, and 20 mol % relative to $[Ti(OCH(CH_3)_2)_4]$) was added to the $[Ti(OCH(CH_3)_2)_4]$/ethyl acetate solution. The precursor flow was kept at 1.4 L·min^{-1}. The substrate temperature was 470 °C. After the precursor solution had been transferred, the bubblers were closed, and the substrate was cooled under a flow of N_2 to less than 100 °C before it was removed. Coated substrates were handled and stored in air. The coated glass substrate was cut into ca. 1 cm × 1 cm squares for subsequent analysis.

Film Characterization. Powder X-ray diffraction (PXRD) patterns were measured using a modified Bruker-AXS D8 diffractometer with parallel beam optics and a PSD LynxEye silicon strip detector. This instrument uses an unmonochromated Cu Kα source (Kα$_1$, 1.54 Å) operated at 40 kV with a 30 mA emission current. The incident beam angle was set at 1°, and the angular range of the patterns collected was $10° < 2\theta < 65°$ with a step size of 0.05° counted at 1 s/step. Raman spectroscopy was carried out on a Renishaw 1000 spectrometer equipped with a 514.5 nm laser. The Raman system was calibrated using a silicon reference. Scanning electron microscopy (SEM) was performed to determine the surface morphology and film thickness using a JEOL JSM-6301F field emission scanning electron microscope at an accelerating voltage of 5 keV. UV–visible (UV–vis) spectroscopy was performed using a PerkinElmer LAMBDA 950 UV/vis/NIR spectrophotometer over a wavelength range of 300–2500 nm. The spectra were referenced against an air background. X-ray photoelectron spectroscopy (XPS) was performed using a Thermo Kα spectrometer with monochromated Al Kα radiation, a dual beam charge compensation system, and a constant pass energy of 50 eV. Survey scans were collected in the range of 0–1200 eV. High-resolution peaks were used for the principal peaks of Ti (2p), O (2p), Cu (2p), C (1s), and Si (2p). The peaks were modeled using sensitivity factors to calculate the film composition. The area underneath these bands is an indication of the element concentration within the region of analysis (spot size 400 µm). Photoluminescence (PL) spectra from 350 to 800 nm were

recorded using an Edinburgh spectrofluorometer equipped with a maximum average power of 5 mW. The excitation wavelength used was 380 nm. The PL signals from 900 to 1600 nm were collected through a Newport Oriel monochromator interfaced with a Newport Merlin lock-in amplifier and detected by a TE-cooled Ge photo-detector. The samples were excited using a 532 nm diode-pumped solid-state laser. The excitation power was 70 mW. The PL spectra were recorded under air and at room temperature.

Transient Absorption Spectroscopy. TAS was used to determine exciton lifetimes at room temperature (~22 °C) from the microsecond to second timescale. Samples were excited using pulsed laser excitation (λ = 355 nm, Opolette 355, pulse width = 6 ns, pulse repetition = 0.8 Hz, laser power = 1.55 mJ·cm^{-2}) through a liquid light guide. A quartz halogen lamp (100 W, Bentham, IL 1) with a stabilized power supply (Bentham, 605) was used as the probe light source. To reduce stray light, scattered light, and sample emission, two monochromators and appropriate optical cutoff filters were placed before and after the sample. The probe light passing through the sample was detected using a Si photodiode (Hamamatsu Photonics, S1722-01). This signal was passed through an amplifier (Costronics Electronics) and then measured using a digital oscilloscope. Decays presented are the average between 100 and 200 laser pulses. Samples were measured inside a gas-tight quartz cell under an argon gas atmosphere.

Functional Testing. The photocatalytic activity was measured by monitoring the photocatalytic decomposition of a model organic pollutant, stearic acid (95%, Sigma-Aldrich). To measure the photocatalytic decomposition of a stearic acid coating, samples were attached to an IR sample holder consisting of an aluminum sheet with a circular hole in the middle. The stearic acid coating was applied from a saturated solution of stearic acid in chloroform (0.05 M) through a dip-coating process. Pilkington NSG Activ glass was used as a benchmark and blank float glass as a control. The breakdown of the C–H bonds in stearic acid was measured using Fourier transform infrared (FTIR) spectroscopy between 2800 and 3000 cm^{-1} using a PerkinElmer Spectrum RX1 FTIR spectrometer. Measurements were taken at 0, 1, 2, 3, 4, 18, and 23 h intervals with the samples irradiated using a 365 nm UVA lamp.

The C–H bonds in stearic acid absorb at 2958 cm^{-1} (C–H stretch CH_3), 2923 cm^{-1} (symmetric C–H stretch CH_2), and 2853 cm^{-1} (asymmetric C–H stretch CH_2). These peaks can be integrated to give an approximate concentration of stearic acid on the surface using a calibration constant (where 1 A·cm^{-1} in the integrated area between 2800 and 3000 cm^{-1} corresponds to approximately 9.7×10^{15} molecules cm^{-2}).[36,37] The rate of removal of stearic acid can thus be measured by monitoring the decrease in IR absorbance. The results are typically expressed in terms of FQE, ξ, defined as the number of molecules degraded per incident photon (units, molecule × photon^{-1}). The light source was a black light-bulb lamp, 2×8 W (Vilmer-Lourmat). The irradiance of the lamp (I = 3.15 mW cm^{-2}) was measured using a UVX radiometer (UVP).

E. coli (ATCC 25922) and *S. aureus* (8325-4) strains were maintained by weekly subculture on Brain Heart Infusion (BHI) agar (Oxoid, Basingstoke, UK). Both bacteria were used to inoculate two separate 10 mL aliquots of sterile BHI broths (Oxoid, Basingstoke, UK) and incubated aerobically at 37 °C for 18 h. Bacteria from the overnight culture were harvested by centrifugation at 13,000g for 1 min. The bacteria were then resuspended in phosphate-buffered saline (PBS) (Oxoid, Basingstoke, UK) and again centrifuged at 13,000g for 1 min. Finally, the bacterial pellet was resuspended in PBS before use. The turbidity of the bacterial cell suspension was measured at 600 nm using a spectrophotometer and was adjusted to an optical density, which corresponded to approximately 10^5 colony-forming units per 25 µL aliquot.

Prior to use, the pure TiO_2 and Cu-doped TiO_2 slides were cut into 1×1 cm sections. A humidity chamber was created to ensure that the suspensions did not dry out. A 25 µL aliquot of the bacterial cell suspension was spread evenly on the surface of each slide and incubated at room temperature (21 ± 2 °C) for the allocated exposure time. For each exposure time (2 and 4 h), triplicate samples
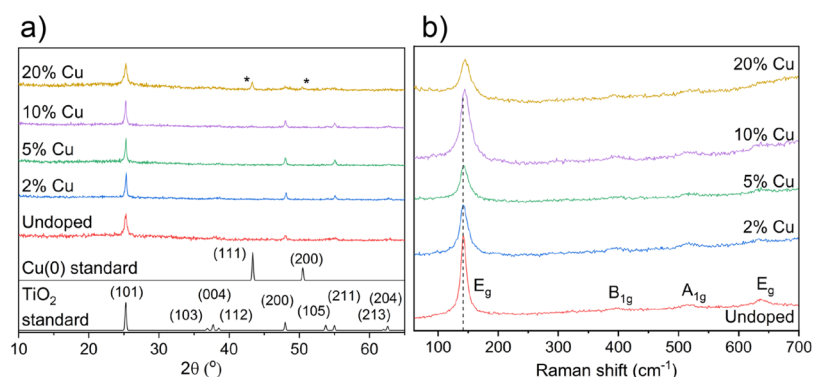
Figure 1. (a) XRD patterns and (b) Raman spectra for the undoped, 2, 5, 10, and 20% Cu-doped TiO_2 anatase films grown using AACVD.
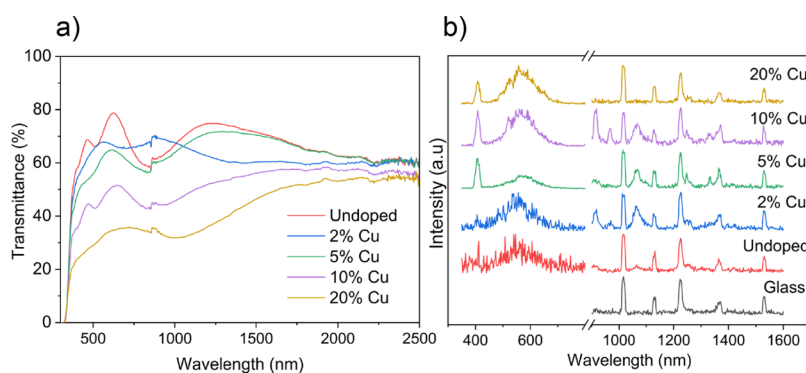
Figure 2. (a) UV−vis spectra encompassing the UV, visible, and near-IR wavelengths and (b) PL spectra for the undoped, 2, 5, 10, and 20% Cu-doped TiO_2 anatase films grown using AACVD.

were analyzed, and uncoated glass microscope slides were used as a control. The samples were then irradiated for 2 and 4 h using a UVA lamp (Vilber-Lourmat, 2×8 W, 365 nm, 0.65 ± 0.23 mW cm^{-2}). A further set of samples (in triplicate) was maintained in the dark for the duration of the irradiation time. Each exposure time was also repeated on two separate occasions.

After incubation, the slides were aseptically transferred to 5 mL of PBS and vortexed for 30 s to release the bacteria into the solution. Serial dilutions of the resulting bacterial suspensions were prepared in PBS, and 100 μL from each dilution was spread onto MacConkey agar (Oxoid, Basingstoke, UK) for *E.coli* and Mannitol salt agar (MSA, Oxoid Ltd) for *S. aureus*. Plates were incubated aerobically at 37 °C for 24 h. After incubation, any bacterial colonies were counted, and viable counts of bacteria were calculated.

Theoretical Methodology. All bulk properties, intrinsic defects, and extrinsic dopants together with their respective charge states were simulated using DFT within the plane-wave code VASP.[36,38−40] Defect supercells were created from the geometrically optimized bulk parameters of anatase TiO_2 using the hybrid HSE06 (Heyd−Scuseria−Ernzerhof)[41,42] functional. Hybrid functionals are an improvement on standard DFT functionals, which contain a systematic self-interaction error, thus underestimating band gaps. HSE06 has been shown to provide a reasonably accurate description of the electronic and geometric properties of all the polymorphs of TiO_2.[2,43−49] In order to describe the interactions between the core and valence electrons, the projector augmented wave (PAW) method[50] was used, which mimics an all-electron method but with greater computational efficiency.

A geometry optimization was carried out on the primitive unit cell of bulk anatase TiO_2, allowing volume, lattice parameters, and atoms to relax until the forces on all the atoms were less than 0.01 eV Å^{-1}. An accurate geometry and electronic structure was calculated using a 450 eV plane-wave energy cutoff and a Γ-centered $7 \times 7 \times 5$ k-point grid. From the primitive bulk, a $3 \times 3 \times 2$ supercell containing 108 atoms was created, and thus defective variants were made. Geometric

optimizations on the supercells were calculated with only the ions allowed to relax until all the forces were less than 0.01 eV Å^{-1}. Γ-centered k-point meshes of $2 \times 2 \times 2$ combined with plane-wave cutoffs of 450 eV were used, and all defect calculations were spin-polarized. It is known that under Ti-rich conditions, Ti_2O_3 is a limiting phase as seen in other theoretical calculations;[51] the geometry and total energy of the relaxed unit cell were calculated using a plane-wave cutoff of 450 eV and a Γ-centered k-point mesh of $8 \times 8 \times 8$. For the Cu chemical potential, three limiting phases were considered: CuO, Cu_2O, and Cu where, under O-poor conditions, the chemical potential is limited by the formation of Cu and, under O-rich conditions, by the formation of CuO. A geometry optimization of CuO was calculated using a plane-wave cutoff of 450 eV and a Γ-centered k-point mesh of $6 \times 6 \times 6$, and the lowest energy magnetic configuration was found to be antiferromagnetic, consistent with other first-principles calculations and experiment.[52−55] See the Supporting Information for methodology on defect formalism, thermodynamic limits, and optical absorption and emission calculations.

■ RESULTS AND DISCUSSION

Pure and Cu-doped TiO_2 films were synthesized from the AACVD reaction of $[Ti(OCH(CH_3)_2)_4]$ and 2, 5, 10, and 20 mol % of $[Cu(NO_3)_2 \cdot 3H_2O]$ in ethyl acetate at 470 °C with N_2 as the carrier gas. All films were translucent with gray/green coloration, particularly the 20 mol % doped film had excellent coverage and well adhered to the substrate, passing the Scotch tape test.[56]

X-ray Diffraction and Raman Spectroscopy. The films were studied using XRD (Figure 1a) to determine whether the desired solid solution had formed. Only reflections for the anatase phase of TiO_2 were visible for all films apart from the 20% doped where, as the possible maximum Cu solubility is
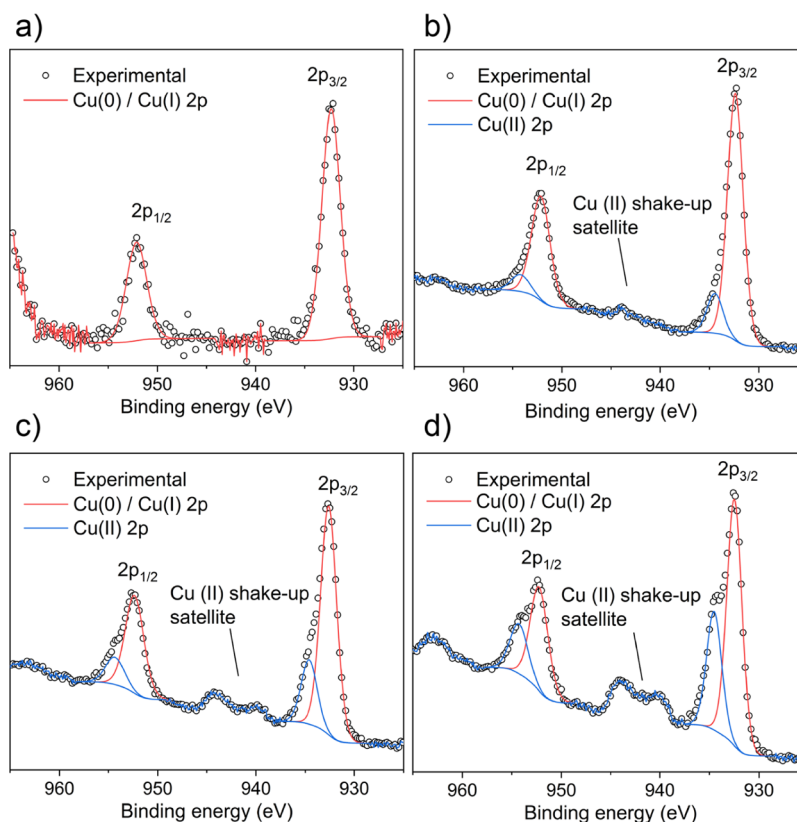
Figure 3. Cu 2p XPS spectra for the (a) 2, (b) 5, (c) 10, and (d) 20% Cu-doped TiO_2 anatase films showing the presence of Cu(0), Cu(I), and Cu(II) oxidation states.

reached, additional peaks (43.2 and 50.4°) corresponding to the Cu metal were also observed. No noticeable shifting of the anatase Bragg reflections was seen for the Cu-doped films that would be normally expected upon substitutional or interstitial doping because of the difference in ionic radius among Ti(IV) (0.60 Å), Cu(I) (0.77 Å), and Cu(II) (0.73 Å). This does introduce the possibility that the Cu dopant may not be present in the lattice, that is, as a solid solution but actually as a secondary phase(s). However, the lack of TiO_2 lattice distortion is explained by the DFT calculations where substitutional Cu doping of anatase is expected to cause minimal distortion of the lattice (see the Defect Thermodynamics section). Raman spectroscopy (Figure 1b) showed only shifts for the tetragonal anatase phase with four active modes visible for all samples including 20%—this is expected as Cu(0) would be Raman inactive. With increasing Cu concentration, the Raman data also showed a small blue shift in the principal E_g vibrational mode (caused by symmetric O—Ti—O stretching vibrations in TiO_2 and indicative of unit cell size) of anatase. This indicates an expansion in the anatase unit cell and is in contrast to XRD results where no change was observed. This discrepancy can be explained by the fact that Raman spectroscopy is more surface-sensitive compared to XRD.

Ultraviolet−Visible Spectroscopy and PL. Figure 2a shows the UV−vis spectra for the pure and Cu-doped films. The spectra are quite similar for pure TiO_2 and 2% Cu-doped TiO_2, with transmittance in the visible region at 70%. The transmittance in the visible region decreases systematically with increasing Cu concentration reaching 30% for the 20% doped film. The indirect optical band gap, calculated using the

Tauc plot, remained at 3.3 eV for the pure, 2, 5, and 10% films. For the 20% Cu-doped TiO_2 film however, a small shift was observed at 3.2 eV (see the Supporting Information).

Figure 2b shows that the emission of Cu-doped TiO_2 films in the UV−vis and IR regions was carried out by PL. PL spectral emission can be used to study charge carrier recombination and to investigate the efficiency of charge carrier trapping, migration, separation, and transfer in semiconductors.[57−59] PL emission spectra result from the radiative recombination of photoexcitation, where a higher PL intensity shows a higher degree of radiative recombination.[57,60] There have been examples of materials displaying strong PL and high photocatalytic activity.[61]

PL emission spectra of Cu-doped TiO_2 at different Cu-doping concentrations (2, 5, 10, and 20%) in the wavelength range from 350 to 800 and 900 to 1600 nm with excitation wavelengths of 380 and 532 nm (respectively) are presented in Figure 2b. All the samples have a peak at 380−430 nm, which could be due to band gap, defects, or surface trapping of electrons.[60] There are broad peaks from around 500 to 650 nm which intensify with increasing Cu doping, and the peaks located at around 520 nm are thought to be due to a self-trapping of electrons by the TiO_6 octahedra.[60] In the NIR region, emission peaks with wavelengths of 1010, 1128, 1230, 1340, and 1525 nm are found to originate as normal glass emissions. In undoped anatase TiO_2, the nonglass peaks exist as low-intensity peaks, in particular peaks around 920 and 1050 nm are likely due to defect-centered emissions. In 2, 5, and 10% Cu-doped anatase, the peaks present in anatase (nonglass) are observed here albeit more pronounced. In 2, 5, and 10% TiO_2:Cu, additional peaks exist such as the
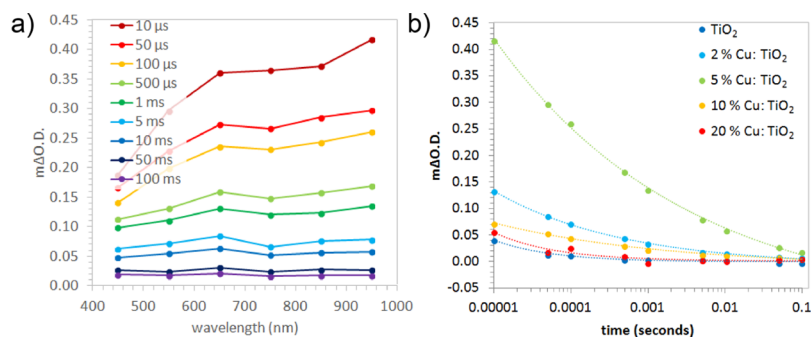
Figure 4. (a) Transient absorption spectra at select times for the 5% Cu-doped TiO$_2$ thin film. (b) Recombination kinetics at 950 nm for all samples, where the dashed lines represent a fit to a power law decay model [$f(t) = a \cdot t^b$, where t is the time and a and b are variables].

emission at 960, 1250, and 1400 nm. 20% Cu, however, appears more like undoped anatase, with the glass peaks dominating the spectrum. To understand these results, theoretical calculations on the PL of Cu-doped anatase are given below (dopant-centered optical properties).

X-ray Photoelectron Spectroscopy. The oxidation state of the Cu dopant on the surface of the films was determined using XPS (Figure 3). In the 2% Cu-doped film, the Cu $2p_{3/2}$ peak is centered at 932.3 eV, matching the transition for Cu(0) and/or Cu(I) [because of heavy peak overlap, it is difficult to distinguish between Cu(0) and Cu(I) from the Cu 2p region alone].[62,63] The lack of the Cu(II) shake-up satellite peak that is normally found around 945 eV indicates the absence of Cu(II) on this surface. For the higher 5, 10, and 20% doped films, the line shapes of the Cu $2p_{3/2}$ and $2p_{1/2}$ transitions are asymmetrical and therefore deconvoluted to two different environments. For these films, the principal $2p_{3/2}$ peaks are centered at 932.4 eV and matches to Cu(0)/Cu(I). The secondary peaks are centered at 934.5 eV and are assigned to Cu(II).[62,63] The presence of Cu(II) here is further supported by the associated satellite peaks at 945 eV. This supports the DFT results which indicate that both Cu(I) and Cu(II) states are expected in both substitutional and interstitial sites in the anatase crystal lattice (see the Defect Thermodynamics section).

The Cu dopant on the surface of the films was determined using the XPS data. For the 0, 2, 5, 10, and 20 mol % solutions used, the concentration of Cu was 0, 22, 30, and 38 at. %, suggesting surface segregation of Cu.

Transient Absorption Spectroscopy. TAS is a form of laser flash spectroscopy that can monitor the generation, recombination, trapping, charge transfer, and so forth of photogenerated charges in semiconductors.[64,65] The dynamics of photogenerated charges can be studied by tracking transient changes in absorbance at particular wavelengths,[66] where it has been shown that the electrons and holes in anatase TiO$_2$ absorb in the visible region.[67,68] The technique has primarily been used to study charge-transfer processes in solar cells (organic–organic or inorganic–organic)[69–71] and has also been used to study charge transfers in heterojunction photocatalysts (inorganic–inorganic)[72] as well as the kinetics of photocatalytic processes.[73–75]

In this study, the kinetics of electron–hole recombination for the series of Cu-doped anatase TiO$_2$ samples were investigated using TAS. Samples were excited using a UVA laser (355 nm, 1.55 mJ·cm^{-2}·per pulse), and the transient changes in absorption were measured from 450 to 950 nm. Previous studies have shown that the photogenerated electrons

and holes in anatase show broad absorptions centered at ~800 and 450 nm, respectively.[67] An example TAS spectrum of the 5% Cu-doped TiO$_2$ sample is shown in Figure 4a, which shows an extended absorption across the visible typical of anatase TiO$_2$. The decay kinetics did not change with probe wavelength. This showed that charge-transfer processes were not occurring within the material. For instance, it has typically been cited that phase-segregated metal dopants in TiO$_2$, such as Cu, may act as electron sinks.[76] If Cu was indeed acting as an electron sink, our TAS studies would show a difference in decay kinetics in the electron region (~800 nm) compared with the hole region (~450 nm). This was not the case for any Cu-doped sample studied herein. As the samples were studied in an argon atmosphere, no photochemistry could occur. This indicated that the transient decay of our absorption signals was due solely to electron–hole recombination. The kinetics of electron–hole recombination were compared across all samples (Figure 4b). These kinetics could be fit to power law decays, typical of the trap/detrapping movement of the charge found in anatase TiO$_2$.[77] The rate of recombination was quantified by finding the time where half the initial absorption was lost ($t_{50\%}$). In the 5% Cu-doped TiO$_2$ sample, recombination was the slowest ($t_{50\%} \approx 110$ ms), followed by the 2% ($t_{50\%} \approx 26$ ms), 10% ($t_{50\%} \approx 19$ ms), 20% ($t_{50\%} \approx 3$ ms), and undoped sample ($t_{50\%} \approx 1$ ms). In the undoped sample, the timescale of recombination was typical of anatase TiO$_2$. Moreover, our TAS results showed that Cu doping resulted in an enhancement in charge carrier lifetime. Substantial differences in the initial absorption were also observed (Figure 4b). This indicated that there were critical differences in ultrafast timescale recombination between samples, not observable on the timescale of these measurements. It was clear that the 5% Cu-doped TiO$_2$ sample possessed the greatest number of photogenerated charges from 10 μs (followed by the 2, 10, 20%, and undoped TiO$_2$ sample). This trend was analogous to the lifetime of photogenerated charges, where the 5% Cu-doped TiO$_2$ samples showed both the most charges from 10 μs and the slowest rate of electron–hole recombination.

Photocatalysis Testing. The photocatalytic activities of the as-synthesized films were evaluated against the degradation of a model organic pollutant, octadecanoic (stearic) acid, under ultraviolet (UVA) illumination ($I = 3.15$ mW cm^{-2}). Stearic acid is highly stable under UV light (in the absence of an underlying effective photocatalyst) and can be easily monitored on transparent materials via infrared spectroscopy. Its photocatalytic degradation can be monitored following the disappearance of characteristic C–H modes at 2958, 2923, and

2853 cm^{-1} (Figure 5b). The photocatalytic rates were estimated from the linear regression of the initial steps (30–
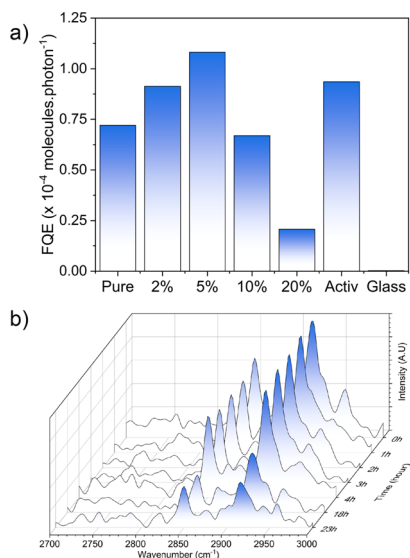

Figure 5. (a) FQEs obtained during the degradation of stearic acid under the UVA irradiation of Cu:TiO$_2$ and undoped thin films. Blank glass and Activ samples are included for comparison. (b) IR spectra of stearic acid upon UVA illumination ($I = 3.15$ mW·cm^{-2}) on a typical Cu-doped TiO$_2$, 5% Cu:TiO$_2$.

40%) of the curve of integrated area versus illumination time. The corresponding rates were expressed as FQEs, defined as molecules of stearic acid degraded over incident photons (units, molecule × photon^{-1}) (Figure 5a). The variation in FQE values was not attributed to differences in physical properties of the films as all films investigated showed comparable thicknesses and crystallinity based on XRD and SEM analyses (Figure 1a and Supporting Information). In addition, a blank piece of glass (as a control) and Pilkington Activ self-cleaning glass (15 nm TiO$_2$ anatase coating) were also tested for comparison.

The pure TiO$_2$ sample showed a destruction rate of 7.2×10^{-5} molecules·photon^{-1}; upon doping 2 and 5% of Cu, the rate increases to 9.1×10^{-5} and 1.1×10^{-4} molecules·photon^{-1} (a higher rate than Activ, 9.4×10^{-5} molecules·photon^{-1}), respectively. At higher concentrations of Cu (10 and 20%), the stearic acid destruction rate decreases to 6.7×10^{-5} and 2.1×10^{-5} molecules·photon^{-1}, respectively. The film photocatalytic activities observed (Figure 5) could be correlated directly with photogenerated charge carrier lifetimes (Figure 4), where high lifetime resulted in high photocatalytic activity. These observations were attributed to the kinetics of the typical processes associated with photocatalysis on TiO$_2$. It is commonly accepted that photocatalysis on TiO$_2$ occurs through the reaction of (i) holes with surface H$_2$O producing highly reactive hydroxyl radicals that subsequently degrade nearby organics and (ii) electrons with O$_2$ forming highly reactive superoxide radicals that also degrade nearby organics.[71] These two processes occur on different timescales, where it has been demonstrated that holes can react with H$_2$O within ~2 μs and electrons react with O$_2$ from 10 to 900 μs.[72] Our TAS studies showed that the sample with the longest-lived photogenerated charge carrier was 5% Cu-doped TiO$_2$, which showed both the slowest rate of recombination and the highest number of photogenerated charges.

Antibacterial Testing. Because the 5% Cu-doped TiO$_2$ sample showed the best photocatalytic results, this sample was chosen along with pure TiO$_2$ for antimicrobial activity testing against a Gram-negative bacterium, *E. coli*, and a Gram-positive bacterium, *S. aureus*, in the dark and under UVA-irradiated conditions. In the case of *E. coli*, there was no significant reduction in the colony counts for the pure TiO$_2$ sample in the dark from 2 to 4 h (Figure 6a,b). A small reduction was observed under UVA irradiation, which is likely due to the
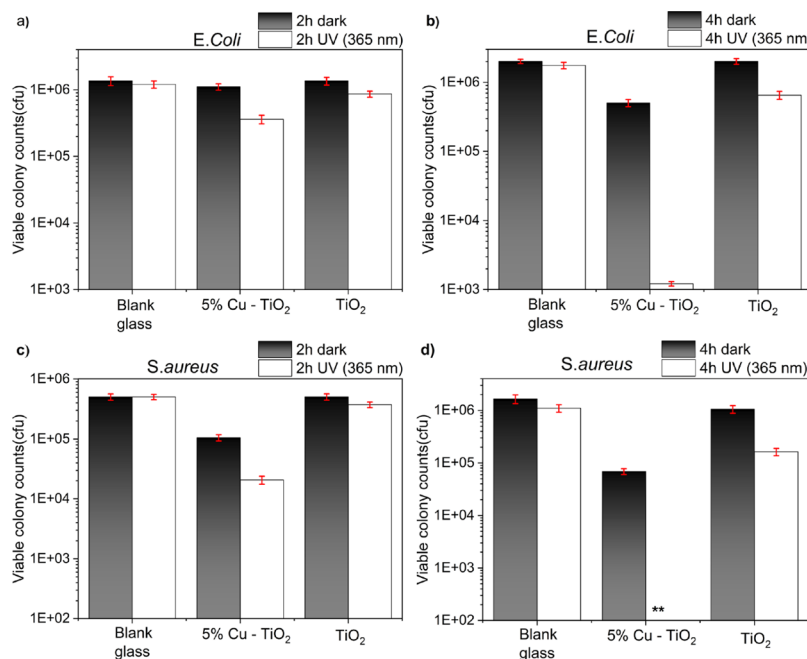
Figure 6. Antimicrobial test results for pure and 5% doped films in the dark and under UVA conditions for 2 (a,c) and 4 h (b,d) against Gram-negative *E. coli* (a,b) and Gram-positive *S. aureus* (c,d) bacteria.
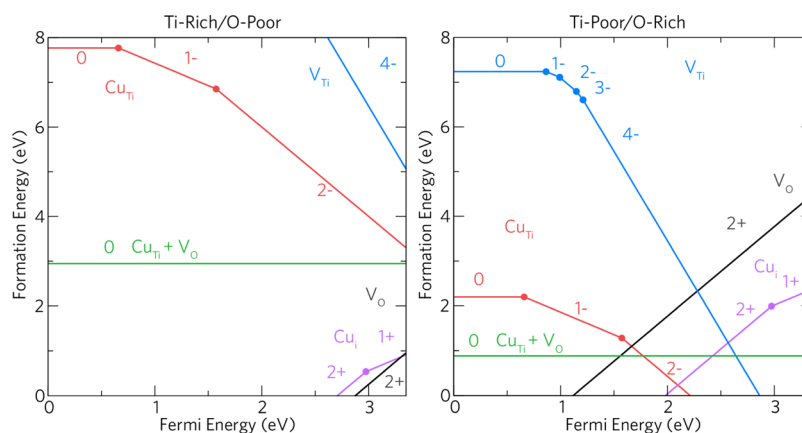
Figure 7. Transition level diagram under both Ti-rich/O-poor (left) and Ti-poor/O-rich (right) growth regimes. The Fermi energy ranges from the VBM (0 eV) to the CBM ($\sim$3.35 eV).

oxidative stress caused by the generation of ROS. This was also observed when the pure TiO_2 sample was tested against *S. aureus* (Figure 6c,d). However, for the Cu-doped sample, there was a small but significant decrease in the colony counts of both *E. coli* and *S. aureus* in the dark, which is possibly due to the cytotoxicity of Cu^0, Cu^+, and Cu^{2+}. Under UVA irradiation of 4 h, there was a rapid decrease in bacterial numbers, to below or almost below detectable levels, for *S. aureus* and *E. coli*, respectively (Figure 6b,d). We attribute this to the generation of ROS that attack organic matter when TiO_2 is irradiated with energy above its band gap as well as the cytotoxicity of Cu species. The activity was higher in the Cu-doped TiO_2 film compared to that in the undoped film, as previously observed from TAS measurements and discussed, because of the Cu states acting as trapping sites that can reduce charge carrier recombination. The lifetimes of the charge carrier are important as they have to travel to the surface of the semiconductor before they can undergo reactions with water and oxygen to produce ROS that then proceed to destroy bacterial cells. The secondary reason for the superior activity of the doped samples over the undoped samples is due to the presence of Cu that has its own antibacterial properties via Fenton-type reactions as discussed in the Introduction. The reasons for the higher killing efficacy for the Gram-positive bacteria *S. aureus* over the Gram-negative *E. coli* are not fully understood, but it may be due to their increased permeability toward cytotoxic Cu ions of the Gram-positive bacteria cell envelope that is composed of a cell membrane and a highly permeable cell wall. Although the cell envelope is thinner for Gram-negative bacteria, it contains two membrane layers of which the outer membrane is constructed of mostly tightly packed lipopolysaccharide molecules that are successful permeability barriers.[78]

Defect Thermodynamics. In order to rationalize the increased performance of the Cu-doped TiO_2 films over the undoped films, we have carried out a detailed hybrid DFT study of the defect chemistry of Cu-doping anatase TiO_2. Figure 7 displays the thermodynamic transition levels for all the intrinsic and extrinsic defects considered in this study under Ti-rich/O-poor and Ti-poor/O-rich conditions.

In this study, the dominant acceptor and donor defects present in anatase TiO_2 are considered. These have been shown in previous theoretical studies to be the oxygen vacancy (V_O) and the titanium vacancy (V_{Ti}).[46,49,51,79−81] Ti-rich/O-poor growth conditions typically favor the formation of n-type

defects, thus V_O is lowest in formation energy under these conditions ($\Delta H_f (V_O^0) = \sim$1.19 eV). Under Ti-poor/O-rich conditions, the formation of an oxygen vacancy rises to $\sim$4.71 eV. V_O acts as a resonant two-electron donor with the 2+/0 transition level occurring $\sim$0.12 eV above the conduction band maximum (CBM). This is in contrast to other wide band gap metal oxides such as ZnO,[82−85] SnO_2,[85−88] and $BaSnO_3$[89,90] where V_O acts as a deep donor and is not expected to contribute largely to the intrinsic conductivity of the material. Our results are consistent with previous theoretical studies on anatase.[49,51,89−92]

The titanium vacancy acts as an ultradeep acceptor with the 0/1− transition level occurring $\sim$0.87 eV above the valence band maximum (VBM). Under typically p-type favorable conditions (Ti-poor/O-rich), the formation energy of the neutral charge state is $\sim$7.23 eV and almost doubles under Ti-rich/O-poor growth conditions ($\Delta H_f (V_{Ti}^0) = \sim$14.26 eV). All holes are localized on adjacent oxygens around the defect as shown in previous calculations.[93] Under a Ti-poor/O-rich regime, V_{Ti}^{4-} begins to compensate V_O^{2+} $\sim$2.28 eV above the VBM trapping the Fermi energy around this point.

Under Ti-poor/O-rich conditions, Cu_{Ti} acts as a relatively low formation energy deep acceptor. The formation energy of Cu_{Ti}^0 is $\sim$2.20 eV, and the 0/1− transition level occurs $\sim$0.65 eV above the VBM. The 1−/2− transition level occurs $\sim$1.57 eV above the VBM, and the 3− charge state is not seen over the entirety of the band gap. Copper is therefore incorporated as Cu(II) when in a substitutional configuration, which explains the prevalence of this oxidation state in the experiment.[21,22,94−96] Figure 8a−c shows the hole localization on and around the Cu_{Ti} defect in the neutral (7c), 1− (7b), and 2− (7c) charge states. In Cu_{Ti}^0, one hole is localized in a d-orbital on Cu and the other two are delocalized on the six joining oxygens. The evolution to the 1− charge state fills a hole with an electron leaving one localized in the Cu d-orbital and the other delocalized as before. In the 2− charge state, (7c), the remaining hole is still mostly localized in the Cu d-orbital but with some density on two equatorial (to the plane of the page) oxygen p-orbitals. Despite being a larger cation than Ti,[97] Cu substitution results in a minimal distortion of the crystal lattice. The Cu atom itself remains in the original Ti position over all charge states, and the adjacent oxygen ions hardly shift from their positions in the neutral, 1−, and 3− charge states. The Cu_{Ti}^{2-} case displays a small shift of one of the O ions by $\sim$10%, as seen in Figure 8c. Cu_{Ti}^{2-} begins to be
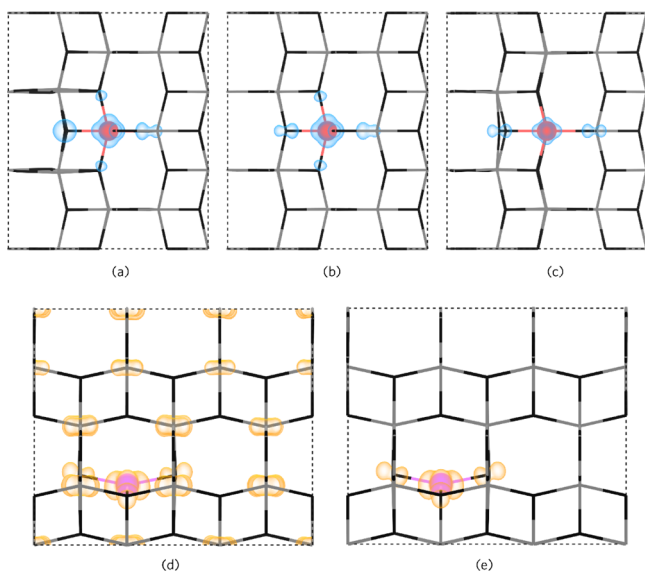
Figure 8. Partial charge densities for the Cu-related defects. (a−c) Hole charge density for Cu^0_{Ti}, Cu^-_{Ti}, and Cu^{2-}_{Ti} defects as viewed along the (010) direction. (d,e) Electron charge density for Cu^0_i and Cu^+_i, respectively, as viewed down the (100) direction. The hole density is shown in blue and the electron density in orange 0−0.015 eV Å^{-1}.

compensated for by V^{2+}_O ∼1.67 eV above the VBM (∼1.68 eV below the CBM) under Ti-poor/O-rich conditions trapping the Fermi energy at this point. Under n-type favorable

conditions, Ti-rich/O-poor, Cu^0_{Ti} has a very high formation energy of ∼7.76 eV and is thus likely to form in negligible quantities.

Our calculations show that the formation energy of Cu_{Ti} is reduced when adjacent to an oxygen vacancy ($[Cu_{Ti} + V_O]$). Under O-poor and O-rich conditions, this defect cluster possesses formation energies of ∼2.94 and ∼0.89 eV, respectively. In $[Cu_{Ti} + V_O]$, Cu relaxes slightly away from V_O compared to Cu in Cu^{2-}_{Ti} as expected. These results indicate however that the presence of this defect cluster is unlikely to appear in large quantities under both Ti-poor/O-rich conditions and that Cu doping will not likely induce oxygen vacancies in anatase TiO_2 consistent with the work by Mathew et al.[98]

Cu_i acts as a resonant one-electron donor under both growth regimes and has a quite low formation energy under Ti-rich/O-poor conditions ($\Delta H_f (Cu^0_i)$ = ∼0.96 eV), which rises to ∼2.41 eV under Ti-poor/O-rich conditions. From our calculations, it is likely that interstitial Cu incorporates as Cu(I) with the 2+/1+ transition level occurring ∼0.37 eV below the CBM. In the literature, Cu is seen as both Cu(II) and Cu(I), and it is likely that both Cu_i and Cu_{Ti} coexist in the anatase lattice, as indicated by our calculations. Despite being a resonant donor, the 1+/0 transition level occurs ∼0.05 eV above the CBM, indicating that increasing the copper incorporation into anatase will not lead to high carrier concentrations. When in the neutral charge state (Cu^0_{Ti}), Cu is expected to exist as Cu^{2+}, thus when the Fermi level is very high, that is, with increased Cu incorporation, Cu^{2+} is expected to be seen (likewise with lower concentrations, Cu^+ may be
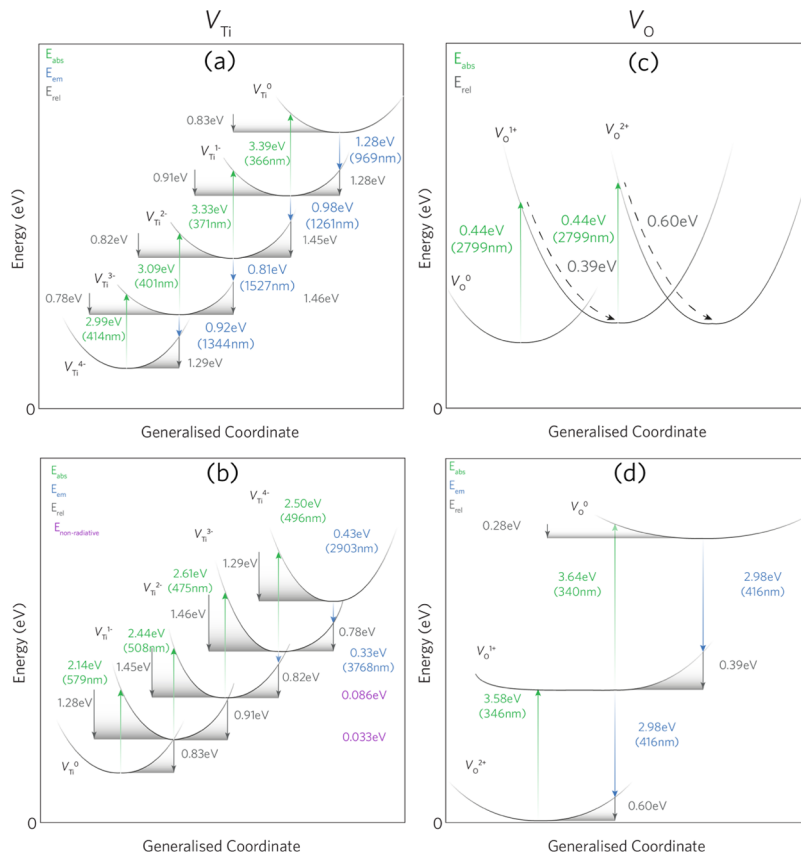
Figure 9. Configurational coordinate diagrams for V_{Ti} (a,b) and V_O (c,d). (a,c) Absorption and subsequent emission of an electron to/from the CBM and (b,d) capture of an electron and subsequent emission from/to the VBM.
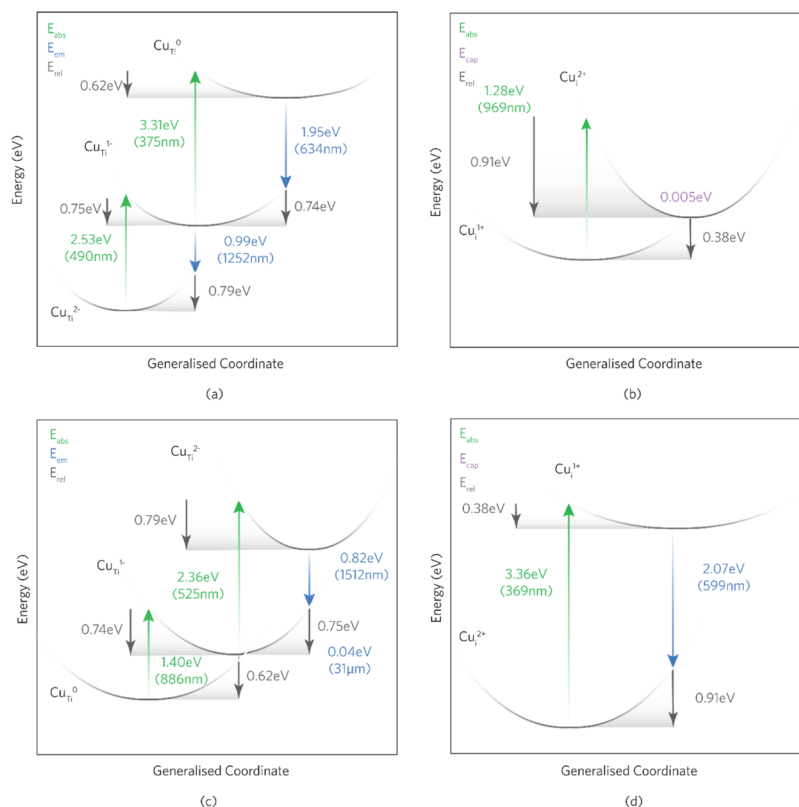
Figure 10. One-dimensional configurational coordinate diagram for (a,c) Cu_{Ti} and (b,d) Cu_i under electron and hole ionization, respectively. In each example, the absorption and emission energies are independent of the chemical potentials and therefore the growth conditions.

seen). From our calculations, Cu_i moves from the perfect octahedral interstitial position to a distorted square planar position where it bonds to four oxygens. This can be seen in Figure 8d,e. This behavior is not surprising considering that Cu^{2+} is well known to be Jahn−Teller active, thus preferring a distorted square planar configuration. Under all charge states, Cu remains in the same position and the Cu−O distances remain at 2.00 Å similar to the average Ti−O bond length of 1.98 Å in anatase. The neighboring four Ti ions move slightly away by an average of 4% from the Cu_i defect and remain in the same position over all the charge states. In Figure 8d,e, the partial charge density is shown for the neutral (Figure 8d) and 1+ (Figure 8e) charge states. In the neutral charge state, both electrons are delocalized over the Ti 3d orbitals that make up the CBM [indicating Cu(II)], and in the 1+ charge state, there is a localization of the electron density on and around Cu [indicating Cu(I)].

Dopant-Centered Optical Properties. The optical transitions for all defects were evaluated and are shown for the intrinsic defects, V_{Ti} and V_O, in Figure 9 and substitutional and interstitial Cu in Figure 10.

Absorption. V_{Ti} undergoes optical absorption from both the excitation of an electron to the conduction band and the ionization of a hole in the valence band and is shown in Figure 9a,b, respectively. For the excitation of an electron to the conduction band, V_{Ti} undergoes four transitions with 414, 401, 371, and 366 nm for $V_{Ti}^{4-} \rightarrow V_{Ti}^{3-}$, $V_{Ti}^{3-} \rightarrow V_{Ti}^{2-}$, $V_{Ti}^{2-} \rightarrow V_{Ti}^{-}$, and $V_{Ti}^{-} \rightarrow V_{Ti}^{0}$, respectively. These absorptions are likely to exist within the absorption edge of anatase and thus will be indistinguishable; however, these may be present in fine structure absorption spectra peaks.[99] V_{Ti} can also undergo the capture of an electron (or hole ionization) from the valence

band, resulting in four more absorptions with wavelengths of 579, 508, 475, and 496 nm for $V_{Ti}^{0} \rightarrow V_{Ti}^{-}$, $V_{Ti}^{-} \rightarrow V_{Ti}^{2-}$, $V_{Ti}^{2-} \rightarrow V_{Ti}^{3-}$, and $V_{Ti}^{3-} \rightarrow V_{Ti}^{4-}$, respectively. It is likely that these peaks will be seen with the increasing concentration of V_{Ti} and that a greater absorption of visible light will be observed.

Figure 9c,d shows the optical absorption values for V_O. Despite V_O being thermodynamically resonant within the conduction band, the optical excitation of electrons can still occur. The optical excitation to the conduction band from $V_O^{0} \rightarrow V_O^{+}$ and $V_O^{+} \rightarrow V_O^{2+}$ is a two-photon process with a very low absorption energy of 2799 nm whose observation is not likely. A similar two-photon absorption is observed for the capture of an electron from the valence band with much larger absorption energies of around 340 nm.

Figure 10a shows that Cu_{Ti} undergoes optical absorption from Cu_{Ti}^{2-} to Cu_{Ti}^{-} and from Cu_{Ti}^{-} to Cu_{Ti}^{0} in the near-UV (490 nm) and the UV (375 nm) regions, respectively, for the excitation of an electron to the conduction band. These absorptions will occur within the absorption edge of anatase TiO_2 and is thus not expected to be distinguishable experimentally. Cu_{Ti} can also undergo hole ionization from the VBM as shown in Figure 10c where the absorptions occur in the NIR (886 nm; $Cu_{Ti}^{0} \rightarrow Cu_{Ti}^{-}$) and the green region (525 nm; $Cu_{Ti}^{-} \rightarrow Cu_{Ti}^{2-}$) of the visible spectrum. These results can be seen in the transmission data in (Figure 2a) by the dip around the absorption edge and ~525 nm compared to undoped pure anatase and is shown to be quite pronounced in the 10% Cu samples, signifying larger concentrations of substitutional Cu.

Figure 10b,d displays the electron and hole ionization transitions for interstitial Cu (Cu_i), respectively. Figure 10b shows that the optical excitation of an electron to the CBM

results in the absorption of a photon in the NIR region (969 nm) for $Cu_i^+ \rightarrow Cu_i^{2+}$. From the transmission data in (Figure 2a), broad troughs are seen ~900−1200 nm for the 10 and 20% Cu samples, suggesting that an increased incorporation of interstitial Cu is present. The broad troughs are indicative of a large relaxation energy[100] (E_{rel}) which for Cu_i^+ to Cu_i^{2+} is ~0.91 eV. A small dip in the transmission occurs for 5% Cu and none at all for 2% Cu, leading to the conclusion that the 2+ → 1+ transition may be suppressed. It is not expected that an optical transition will occur from the 1+ to the 0 charge states as thermal ionization occurs in the conduction band and has thus been omitted from this diagram. The capture of an electron by Cu_i^{2+} (from the VBM) facilitates the absorption of a photon in the near-UV with a wavelength of which, as with Cu_{Ti}, is not expected to be distinguishable experimentally because of its position in the absorption edge of TiO_2.

Emission. The intrinsic defect emissions for V_{Ti} and V_O are shown in Figure 9. Infrared PL also occurs under both electron excitation and capture. Under electron excitation from V_{Ti} to the conduction band, it is expected for the transitions: $V_{Ti}^0 \rightarrow V_{Ti}^-$, $V_{Ti}^- \rightarrow V_{Ti}^{2-}$, $V_{Ti}^{2-} \rightarrow V_{Ti}^{3-}$, and $V_{Ti}^{3-} \rightarrow V_{Ti}^{4-}$ that emissions of 969, 1261, 1527, and 1344 nm will be seen. Under the emission of an electron to the VBM (Figure 9b), two IR emissions are observed at 2903 and 3768 nm for $V_{Ti}^{4-} \rightarrow V_{Ti}^{3-}$ and $V_{Ti}^{3-} \rightarrow V_{Ti}^{2-}$, respectively. The other transitions are likely to be nonradiative as they occur at very small energies (0.033−0.086 eV). Most experimental PL studies are carried out in the UV−vis region of the electromagnetic spectrum and (<900 nm) and are thus not accounted for in the scientific literature. One study on TiO_2 nanoribbons, however, shows a PL peak of around 969 nm.[101] The Stokes shifts for each transition (difference between absorption and emission) are fairly large and as such indicate a broad shift between the absorption and emission. The total Stokes shifts for each transition: $V_{Ti}^{4-} \leftrightarrow V_{Ti}^{3-}$, $V_{Ti}^{3-} \leftrightarrow V_{Ti}^{2-}$, $V_{Ti}^{2-} \leftrightarrow V_{Ti}^-$, and $V_{Ti}^- \leftrightarrow V_{Ti}^0$ are 2.07, 2.28, 2.36, and 2.11 eV, respectively. Within the PL of Cu-doped TiO_2 in Figure 2b, the peaks at 969, 1250, and 1340 nm correspond to those by V_{Ti}. It is likely that the glass emission around 1531 nm masks the 1527 nm peak from the $V_{Ti}^{2-} \rightarrow V_{Ti}^{3-}$ transition.

V_O only undergoes PL via the release of an electron to the VBM. This is a two-photon process with a wavelength of 416 nm; thus, the peak intensity is expected to be larger than that of a single photon process. Numerous room-temperature studies observe a peak of around 427−417 nm (where a shift is expected at increasing temperature) which Kernazhitsky et al. identify as an oxygen vacancy-related peak.[99,102−106] In Figure 2b, the peak at 416 nm matches well to that calculated here. The intensity of the peak rises with increasing Cu doping, indicating the formation of oxygen vacancies. The total Stokes shift for the two-electron process is calculated as 1.26 eV, in good agreement with the study of Wang et al., which shows a Stokes shift of 1.36 eV.[102]

The emission energies present for electron (Figure 10a) and hole (Figure 10c) ionization of Cu_{Ti} range from the mid-IR region to the red region of the visible spectrum. In Figure 10a, the transition of $Cu_{Ti}^0 \rightarrow Cu_{Ti}^-$ and the subsequent transition of Cu_{Ti}^- to Cu_{Ti}^{2-} give rise to PL peaks at ~ 634 and ~1252 nm, respectively. Upon the release of a hole to the VBM, two PL peaks are expected around 1512 nm ($Cu_{Ti}^{2-} \rightarrow Cu_{Ti}^-$) and ~31 μm ($Cu_{Ti}^- \rightarrow Cu_{Ti}^0$). The latter absorption is expected to be nonradiative because of the very small emission energy and will thus be dissipated through the anatase lattice as

phonons.[107] Similar behavior is seen in acceptor defects such as V_{Zn} in ZnO[108] as well as V_{Ga} in GaN.[107] It is expected that these peaks will be broad because of the relatively large E_{rel} values (~0.7 eV). Because of the glass emission at 1525 nm in Figure 2b, it is hard to tell whether this peak is present in the AACVD-made Cu-doped TiO_2 thin films.

Cu_i will only photoluminesce after the capture of an electron from the valence band. Figure 10b depicts this with a value of 599 nm and a broad peak (E_{rel} = 0.91 eV). This is seen in the room-temperature PL data in (Figure 2b) from ~450 to 625 nm. The highest intensity PL occurs in the 20% Cu sample, which, together with the transmission data in (Figure 2a), indicates that the presence of interstitial Cu is more substantial. Figure 10b shows that Cu_i will not photoluminesce after electron ionization because of the thermodynamic resonance of Cu_i^+ in the conduction band. Instead, it is likely that Cu_i^+ will readily capture an electron with an energy barrier of 0.005 eV to return to the 2+ charge state.

The presence of interstitial Cu in the anatase lattice together with substitutional Cu is likely beneficial to both the photocatalytic activity and the electron-carrier separation lifetimes. The mechanism of this is possibly due to the synergistic effect of deep acceptor/shallow donor pairs whereby an excited electron from Cu_{Ti} can be readily accepted by an interstitial Cu defect, thereby increasing the separation. Electron capture by substitutional Cu occurs in the visible/NIR region of the spectrum ($Cu_{Ti}^0 \rightarrow Cu_{Ti}^-$; E_{abs} = 886 nm), and electron excitation of Cu_i also occurs in the visible/NIR region ($Cu_i^+ \rightarrow Cu_i^{2+}$; E_{abs} = 969 nm) aiding the visible light-enhanced photocatalytic activity. It is possible that competition between these defects may arise with increased Cu incorporation favoring the formation of interstitial Cu over substitutional Cu, thereby losing the beneficial synergistic effect. This is evidenced through the detrimental effect to the carrier separation lifetimes in Figure 4 and to the decrease in photocatalytic activity (Figure 5a) toward higher doping levels where the Cu_{Ti}:Cu_i ratio is suggested to be higher (10 and 20%).

CONCLUSIONS

AACVD provides a facile route to highly photoactive and antimicrobial Cu-doped TiO_2 thin films. From experimental analysis, the 5% TiO_2:Cu film in particular displayed the greatest exciton lifetimes, photocatalytic activity (in the degradation of stearic acid), and antibacterial activity (against *E. coli* and *S. aureus*) under 365 nm irradiation. Using hybrid DFT calculations, this was demonstrated to be due to a synergistic effect from interstitial and substitutional Cu within the anatase lattice and confirmed by optical transmission and PL experiments. Effective dopant selection and concentration control are therefore key to providing the maximum efficiency in terms of carrier lifetimes for migration to the surface for the necessary reactions to take place for photocatalysis and antibacterial activity.

ASSOCIATED CONTENT

Supporting Information
The Supporting Information is available free of charge at https://pubs.acs.org/doi/10.1021/acsami.9b22056.

Defect formalism, thermodynamic limits, and optical calculations and SEM of the Cu-doped TiO_2 films (PDF)

AUTHOR INFORMATION

Corresponding Authors

David O. Scanlon — *Department of Chemistry, Christopher Ingold Building and Thomas Young Centre, University College London, London WC1H 0AJ, U.K.; Diamond Light Source Ltd., Didcot, Oxfordshire OX11 0DE, U.K.;* orcid.org/0000-0001-9174-8601; Email: d.scanlon@ucl.ac.uk; Fax: (+44) 20-7679-7463

Ivan P. Parkin — *Materials Chemistry Centre, Department of Chemistry, University College London, London WC1H 0AJ, U.K.;* Email: i.p.parkin@ucl.ac.uk

Authors

Abdullah M. Alotaibi — *Materials Chemistry Centre, Department of Chemistry, University College London, London WC1H 0AJ, U.K.; The National Centre for Building and Construction Technology, King Abdulaziz City for Science and Technology (KACST), Riyadh 11442-6086, Saudi Arabia*

Benjamin A. D. Williamson — *Department of Chemistry, Christopher Ingold Building and Thomas Young Centre, University College London, London WC1H 0AJ, U.K.;* orcid.org/0000-0002-6242-1121

Sanjayan Sathasivam — *Materials Chemistry Centre, Department of Chemistry, University College London, London WC1H 0AJ, U.K.;* orcid.org/0000-0002-5206-9558

Andreas Kafizas — *, London SW7 2AZ, U.K.;* orcid.org/0000-0002-2282-4639

Mahdi Alqahtani — *Electronic & Electrical Engineering, University College London, London WC1E 7JE, U.K.; Materials Science Research Institute, King Abdulaziz City for Science and Technology (KACST), Riyadh 11442-6086, Saudi Arabia;* orcid.org/0000-0002-9353-1411

Carlos Sotelo-Vazquez — *Materials Chemistry Centre, Department of Chemistry, University College London, London WC1H 0AJ, U.K.*

John Buckeridge — *School of Engineering, London South Bank University, London SE1 0AA, U.K.*

Jiang Wu — *Electronic & Electrical Engineering, University College London, London WC1E 7JE, U.K.; University of Electronic Science and Technology of China, Chengdu 610054, China;* orcid.org/0000-0003-0679-6196

Sean P. Nair — *Department of Microbial Diseases, UCL Eastman Dental Institute, London WC1X 8LD, U.K.*

Complete contact information is available at:
https://pubs.acs.org/10.1021/acsami.9b22056

Notes

The authors declare no competing financial interest.

REFERENCES

(1) Linsebigler, A. L.; Lu, G.; Yates, J. T. Photocatalysis on TiO$_2$ Surfaces: Principles, Mechanisms, and Selected Results. *Chem. Rev.* **1995**, *95*, 735−758.

(2) Scanlon, D. O.; Dunnill, C. W.; Buckeridge, J.; Shevlin, S. A.; Logsdail, A. J.; Woodley, S. M.; Catlow, C. R. A.; Powell, M. J.; Palgrave, R. G.; Parkin, I. P.; Watson, G. W.; Keal, T. W.; Sherwood, P.; Walsh, A.; Sokol, A. A. Band alignment of rutile and anatase TiO$_2$. *Nat. Mater.* **2013**, *12*, 798.

(3) McCullagh, C.; Robertson, J. M. C.; Bahnemann, D. W.; Robertson, P. K. J. The application of TiO$_2$ photocatalysis for disinfection of water contaminated with pathogenic micro-organisms: a review. *Res. Chem. Intermed.* **2007**, *33*, 359−375.

(4) Hashimoto, K.; Irie, H.; Fujishima, A. TiO$_2$ photocatalysis: a historical overview and future prospects. *Jpn. J. Appl. Phys.* **2005**, *44*, 8269.

(5) Georgekutty, R.; Seery, M. K.; Pillai, S. C. A highly efficient Ag-ZnO photocatalyst: synthesis, properties, and mechanism. *J. Phys. Chem. C* **2008**, *112*, 13563−13570.

(6) Morrison, S. R.; Freund, T. Chemical role of holes and electrons in ZnO photocatalysis. *J. Chem. Phys.* **1967**, *47*, 1543−1551.

(7) Ali, T. T.; Narasimharao, K.; Parkin, I. P.; Carmalt, C. J.; Sathasivam, S.; Basahel, S. N.; Bawaked, S. M.; Al-Thabaiti, S. A. Effect of pretreatment temperature on the photocatalytic activity of microwave irradiated porous nanocrystalline ZnO. *New J. Chem.* **2015**, *39*, 321−332.

(8) Promdet, P.; Quesada-Cabrera, R.; Sathasivam, S.; Li, J.; Jiamprasertboon, A.; Guo, J.; Taylor, A.; Carmalt, C. J.; Parkin, I. P. High Defect Nanoscale ZnO Films with Polar Facets for Enhanced Photocatalytic Performance. *ACS Appl. Nano Mater.* **2019**, *2*, 2881−2889.

(9) Hassan, I. A.; Sathasivam, S.; Nair, S. P.; Carmalt, C. J. Antimicrobial properties of copper-doped ZnO coatings under darkness and white light illumination. *ACS Omega* **2017**, *2*, 4556−4562.

(10) Li, Y.; Zhang, W.; Niu, J.; Chen, Y. Mechanism of photogenerated reactive oxygen species and correlation with the antibacterial properties of engineered metal-oxide nanoparticles. *ACS Nano* **2012**, *6*, 5164−5173.

(11) Chadwick, N. P.; Glover, E. N. K.; Sathasivam, S.; Basahel, S. N.; Althabaiti, S. A.; Alyoubi, A. O.; Parkin, I. P.; Carmalt, C. J. Photo-activity and low resistivity in N/Nb Co-doped TiO$_2$ thin films by combinatorial AACVD. *J. Mater. Chem. A* **2016**, *4*, 407−415.

(12) Musat, V.; Teixeira, B.; Fortunato, E.; Monteiro, R. C. C.; Vilarinho, P. Al-doped ZnO thin films by sol−gel method. *Surf. Coating.* **2004**, *180−181*, 659−662.

(13) Matsubara, K.; Fons, P.; Iwata, K.; Yamada, A.; Sakurai, K.; Tampo, H.; Niki, S. ZnO transparent conducting films deposited by pulsed laser deposition for solar cell applications. *Thin Solid Films* **2003**, *431−432*, 369−372.

(14) Page, K.; Palgrave, R. G.; Parkin, I. P.; Wilson, M.; Savin, S. L. P.; Chadwick, A. V. Titania and silver−titania composite films on glass—potent antimicrobial coatings. *J. Mater. Chem.* **2007**, *17*, 95−104.

(15) Wu, B.; Huang, R.; Sahu, M.; Feng, X.; Biswas, P.; Tang, Y. J. Bacterial responses to Cu-doped TiO$_2$ nanoparticles. *Sci. Total Environ.* **2010**, *408*, 1755−1758.

(16) Jaimy, K. B.; Safeena, V. P.; Ghosh, S.; Hebalkar, N. Y.; Warrier, K. G. K. Photocatalytic activity enhancement in doped titanium dioxide by crystal defects. *Dalton Trans.* **2012**, *41*, 4824−4832.

(17) Choi, W.; Termin, A.; Hoffmann, M. R. The Role of Metal Ion Dopants in Quantum-Sized TiO_2: Correlation between Photoreactivity and Charge Carrier Recombination Dynamics. *J. Phys. Chem. A* **1994**, *98*, 13669−13679.

(18) Hassan, I. A.; Parkin, I. P.; Nair, S. P.; Carmalt, C. J. Antimicrobial activity of copper and copper(I) oxide thin films deposited via aerosol-assisted CVD. *J. Mater. Chem. B* **2014**, *2*, 2855−2860.

(19) Ruparelia, J. P.; Chatterjee, A. K.; Duttagupta, S. P.; Mukherji, S. Strain specificity in antimicrobial activity of silver and copper nanoparticles. *Acta Biomater.* **2008**, *4*, 707−716.

(20) You, M.; Kim, T. G.; Sung, Y.-M. Synthesis of Cu-doped TiO_2 nanorods with various aspect ratios and dopant concentrations. *Cryst. Growth Des.* **2010**, *10*, 983−987.

(21) Colón, G.; Maicu, M.; Hidalgo, M. C.; Navío, J. A. Cu-doped TiO_2 systems with improved photocatalytic activity. *Appl. Catal., B* **2006**, *67*, 41−51.

(22) Choudhury, B.; Dey, M.; Choudhury, A. Defect generation, d-d transition, and band gap reduction in Cu-doped TiO_2 nanoparticles. *Int. Nano Lett.* **2013**, *3*, 25.

(23) Park, H. S.; Kim, D. H.; Kim, S. J.; Lee, K. S. The photocatalytic activity of 2.5 wt% Cu-doped TiO_2 nano powders synthesized by mechanical alloying. *J. Alloys Compd.* **2006**, *415*, 51−55.

(24) Celik, E.; Gokcen, Z.; Ak Azem, N. F.; Tanoglu, M.; Emrullahoglu, O. F. Processing, characterization and photocatalytic properties of Cu doped TiO_2 thin films on glass substrate by sol−gel technique. *Mater. Sci. Eng., B* **2006**, *132*, 258−265.

(25) Zhang, W.; Li, Y.; Zhu, S.; Wang, F. Copper doping in titanium oxide catalyst film prepared by dc reactive magnetron sputtering. *Catal. Today* **2004**, *93−95*, 589−594.

(26) Sathasivam, S.; Arnepalli, R. R.; Kumar, B.; Singh, K. K.; Visser, R. J.; Blackman, C. S.; Carmalt, C. J. Solution Processing of GaAs Thin Films for Photovoltaic Applications. *Chem. Mater.* **2014**, *26*, 4419−4424.

(27) Sathasivam, S.; Arnepalli, R. R.; Singh, K. K.; Visser, R. J.; Blackman, C. S.; Carmalt, C. J. A solution based route to GaAs thin films from As (NMe 2) 3 and GaMe 3 for solar cells. *RSC Adv.* **2015**, *5*, 11812−11817.

(28) Alotaibi, A. M.; Sathasivam, S.; Nair, S. P.; Parkin, I. P. Antibacterial properties of Cu−ZrO 2 thin films prepared via aerosol assisted chemical vapour deposition. *J. Mater. Chem. B* **2016**, *4*, 666−671.

(29) Bhachu, D. S.; Moniz, S. J. A.; Sathasivam, S.; Scanlon, D. O.; Walsh, A.; Bawaked, S. M.; Mokhtar, M.; Obaid, A. Y.; Parkin, I. P.; Tang, J.; Carmalt, C. J. Bismuth oxyhalides: synthesis, structure and photoelectrochemical activity. *Chem. Sci.* **2016**, *7*, 4832−4841.

(30) Chadwick, N.; Sathasivam, S.; Kafizas, A.; Bawaked, S. M.; Obaid, A. Y.; Al-Thabaiti, S.; Basahel, S. N.; Parkin, I. P.; Carmalt, C. J. Combinatorial aerosol assisted chemical vapour deposition of a photocatalytic mixed SnO_2/TiO_2 thin film. *J. Mater. Chem. A* **2014**, *2*, 5108−5116.

(31) Sathasivam, S.; Kafizas, A.; Ponja, S.; Chadwick, N.; Bhachu, D. S.; Bawaked, S. M.; Obaid, A. Y.; Al-Thabaiti, S.; Basahel, S. N.; Carmalt, C. J.; Parkin, I. P. Combinatorial Atmospheric Pressure CVD of a Composite TiO_2/SnO_2 Thin Film. *Chem. Vap. Depos.* **2014**, *20*, 69−79.

(32) Ponja, S. D.; Sathasivam, S.; Parkin, I. P.; Carmalt, C. J. Transparent conductive aluminium and fluorine co-doped zinc oxide films via aerosol assisted chemical vapour deposition. *RSC Adv.* **2014**, *4*, 49723−49728.

(33) Knapp, C. E.; Carmalt, C. J. Solution based CVD of main group materials. *Chem. Soc. Rev.* **2016**, *45*, 1036−1064.

(34) Alotaibi, A. M.; Sathasivam, S.; Williamson, B. A. D.; Kafizas, A.; Sotelo-Vazquez, C.; Taylor, A.; Scanlon, D. O.; Parkin, I. P. Chemical vapor deposition of photocatalytically active pure brookite TiO_2 thin films. *Chem. Mater.* **2018**, *30*, 1353−1361.

(35) Ponja, S. D.; Williamson, B. A. D.; Sathasivam, S.; Scanlon, D. O.; Parkin, I. P.; Carmalt, C. J. Enhanced electrical properties of

antimony doped tin oxide thin films deposited via aerosol assisted chemical vapour deposition. *J. Mater. Chem. C* **2018**, *6*, 7257−7266.

(36) Kresse, G.; Hafner, J. Ab initio molecular dynamics for liquid metals. *Phys. Rev. B: Condens. Matter Mater. Phys.* **1993**, *47*, 558.

(37) Mills, A.; Wang, J. Simultaneous monitoring of the destruction of stearic acid and generation of carbon dioxide by self-cleaning semiconductor photocatalytic films. *J. Photochem. Photobiol., A* **2006**, *182*, 181−186.

(38) Kresse, G.; Hafner, J. Ab initio molecular-dynamics simulation of the liquid-metal−amorphous-semiconductor transition in germanium. *Phys. Rev. B: Condens. Matter Mater. Phys.* **1994**, *49*, 14251.

(39) Kresse, G.; Furthmüller, J. Efficiency of ab-initio total energy calculations for metals and semiconductors using a plane-wave basis set. *Comput. Mater. Sci.* **1996**, *6*, 15−50.

(40) Kresse, G.; Furthmüller, J. Efficient iterative schemes for ab initio total-energy calculations using a plane-wave basis set. *Phys. Rev. B: Condens. Matter Mater. Phys.* **1996**, *54*, 11169.

(41) Paier, J.; Marsman, M.; Hummer, K.; Kresse, G.; Gerber, I. C.; Ángyán, J. G. Screened hybrid density functionals applied to solids. *J. Chem. Phys.* **2006**, *124*, 154709.

(42) Heyd, J.; Scuseria, G. E.; Ernzerhof, M. Hybrid functionals based on a screened Coulomb potential. *J. Chem. Phys.* **2003**, *118*, 8207−8215.

(43) Buckeridge, J.; Butler, K. T.; Catlow, C. R. A.; Logsdail, A. J.; Scanlon, D. O.; Shevlin, S. A.; Woodley, S. M.; Sokol, A. A.; Walsh, A. Polymorph engineering of TiO_2: demonstrating how absolute reference potentials are determined by local coordination. *Chem. Mater.* **2015**, *27*, 3844−3851.

(44) Çelik, V.; Mete, E. Range-separated hybrid exchange-correlation functional analyses of anatase TiO_2 doped with W, N, S, W/N, or W/S. *Phys. Rev. B: Condens. Matter Mater. Phys.* **2012**, *86*, 205112.

(45) Huy, H. A.; Aradi, B.; Frauenheim, T.; Deák, P. Calculation of carrier-concentration-dependent effective mass in Nb-doped anatase crystals of TiO_2. *Phys. Rev. B: Condens. Matter Mater. Phys.* **2011**, *83*, 155201.

(46) Janotti, A.; Varley, J.; Rinke, P.; Umezawa, N.; Kresse, G.; Van de Walle, C. Hybrid functional studies of the oxygen vacancy in TiO_2. *Phys. Rev. B: Condens. Matter Mater. Phys.* **2010**, *81*, 085212.

(47) Bhachu, D. S.; Sathasivam, S.; Sankar, G.; Scanlon, D. O.; Cibin, G.; Carmalt, C. J.; Parkin, I. P.; Watson, G. W.; Bawaked, S. M.; Obaid, A. Y.; Al-Thabaiti, S.; Basahel, S. N. Solution processing route to multifunctional titania thin films: Highly conductive and photcatalytically active Nb: TiO_2. *Adv. Funct. Mater.* **2014**, *24*, 5075−5085.

(48) Matsubara, M.; Saniz, R.; Partoens, B.; Lamoen, D. Doping anatase TiO 2 with group Vb and VI-b transition metal atoms: a hybrid functional first-principles study. *Phys. Chem. Chem. Phys.* **2017**, *19*, 1945−1952.

(49) Boonchun, A.; Reunchan, P.; Umezawa, N. Energetics of native defects in anatase TiO_2: a hybrid density functional study. *Phys. Chem. Chem. Phys.* **2016**, *18*, 30040−30046.

(50) Blöchl, P. E. Projector augmented-wave method. *Phys. Rev. B: Condens. Matter Mater. Phys.* **1994**, *50*, 17953.

(51) Morgan, B. J.; Watson, G. W. Intrinsic n-type defect formation in TiO_2: a comparison of rutile and anatase from GGA+ U calculations. *J. Phys. Chem. C* **2010**, *114*, 2321−2328.

(52) Rocquefelte, X.; Schwarz, K.; Blaha, P. Theoretical investigation of the magnetic exchange interactions in copper (II) oxides under chemical and physical pressures. *Sci. Rep.* **2012**, *2*, 759.

(53) Kuz'menko, A. B.; Van Der Marel, D.; Van Bentum, P. J. M.; Tishchenko, E. A.; Presura, C.; Bush, A. A. Phonon anomalies versus magnetic ordering in CuO. *Phys. B* **2000**, *284−288*, 1396−1397.

(54) Scanlon, D. O.; Morgan, B. J.; Watson, G. W.; Walsh, A. Acceptor levels in p-type Cu 2 O: rationalizing theory and experiment. *Phys. Rev. Lett.* **2009**, *103*, 096405.

(55) Scanlon, D. O.; Morgan, B. J.; Watson, G. W. Modeling the polaronic nature of p-type defects in Cu 2 O: The failure of GGA and GGA+ U. *J. Chem. Phys.* **2009**, *131*, 124703.

(56) Mittal, K. L. Adhesion measurement of thin films. *Act. Passive Electron. Components* **1976**, *3*, 21−42.

(57) Lim, S. P.; Pandikumar, A.; Lim, H. N.; Ramaraj, R.; Huang, N. M. Boosting photovoltaic performance of dye-sensitized solar cells using silver nanoparticle-decorated N, S-Co-doped-TiO$_2$ photoanode. *Sci. Rep.* **2015**, *5*, 11922.

(58) Patel, S. K. S.; Gajbhiye, N. S. Room temperature magnetic properties of Cu-doped titanate, TiO$_2$ (B) and anatase nanorods synthesized by hydrothermal method. *Mater. Chem. Phys.* **2012**, *132*, 175−179.

(59) Hasan, M. R.; Suhaimya, S. H. M.; Matb, A. N. C. A sol−gel derived, copper-doped, titanium dioxide−reduced graphene oxide nanocomposite electrode for the photoelectrocatalytic reduction of CO$_2$ to methanol and formic acid. *RSC Adv.* **2015**, *5*, 77803.

(60) Karunakaran, C.; Abiramasundari, G.; Gomathisankar, P.; Manikandan, G.; Anandi, V. Cu-doped TiO$_2$ nanoparticles for photocatalytic disinfection of bacteria under visible light. *J. Colloid Interface Sci.* **2010**, *352*, 68−74.

(61) Liqiang, J.; Xiaojun, S.; Baifu, X.; Baiqi, W.; Weimin, C.; Honggang, F. The preparation and characterization of La doped TiO$_2$ nanoparticles and their photocatalytic activity. *J. Solid State Chem.* **2004**, *177*, 3375−3382.

(62) Biesinger, M. C.; Lau, L. W. M.; Gerson, A. R.; Smart, R. S. C. Resolving surface chemical states in XPS analysis of first row transition metals, oxides and hydroxides: Sc, Ti, V, Cu and Zn. *Appl. Surf. Sci.* **2010**, *257*, 887−898.

(63) Deroubaix, G.; Marcus, P. X-ray photoelectron spectroscopy analysis of copper and zinc oxides and sulphides. *Surf. Interface Anal.* **1992**, *18*, 39−46.

(64) Pesci, F. M.; Cowan, A. J.; Alexander, B. D.; Durrant, J. R.; Klug, D. R. Charge carrier dynamics on mesoporous WO$_3$ during water splitting. *J. Phys. Chem. Lett.* **2011**, *2*, 1900−1903.

(65) Pendlebury, S. R.; Wang, X.; Le Formal, F.; Cornuz, M.; Kafizas, A.; Tilley, S. D.; Grätzel, M.; Durrant, J. R. Ultrafast charge carrier recombination and trapping in hematite photoanodes under applied bias. *J. Am. Chem. Soc.* **2014**, *136*, 9854−9857.

(66) Fujishima, A.; Zhang, X.; Tryk, D. TiO$_2$ photocatalysis and related surface phenomena. *Surf. Sci. Rep.* **2008**, *63*, 515−582.

(67) Wang, X.; Kafizas, A.; Li, X.; Moniz, S. J. A.; Reardon, P. J. T.; Tang, J.; Parkin, I. P.; Durrant, J. R. Transient absorption spectroscopy of anatase and rutile: the impact of morphology and phase on photocatalytic activity. *J. Phys. Chem. C* **2015**, *119*, 10439−10447.

(68) Kafizas, A.; Wang, X.; Pendlebury, S. R.; Barnes, P.; Ling, M.; Sotelo-Vazquez, C.; Quesada-Cabrera, R.; Li, C.; Parkin, I. P.; Durrant, J. R. Where do photogenerated holes go in anatase: rutile TiO$_2$ A transient absorption spectroscopy study of charge transfer and lifetime. *J. Phys. Chem. A* **2016**, *120*, 715−723.

(69) Wang, L.; McCleese, C.; Kovalsky, A.; Zhao, Y.; Burda, C. Femtosecond time-resolved transient absorption spectroscopy of CH$_3$NH$_3$PbI$_3$ perovskite films: evidence for passivation effect of PbI$_2$. *J. Am. Chem. Soc.* **2014**, *136*, 12205−12208.

(70) Clarke, T.; Ballantyne, A.; Jamieson, F.; Brabec, C.; Nelson, J.; Durrant, J. Transient absorption spectroscopy of charge photo-generation yields and lifetimes in a low bandgap polymer/fullerenefilm. *Chem. Commun.* **2008**, 89.

(71) Anderson, L. J. E.; Mayer, K. M.; Fraleigh, R. D.; Yang, Y.; Lee, S.; Hafner, J. H. Quantitative measurements of individual gold nanoparticle scattering cross sections. *J. Phys. Chem. C* **2010**, *114*, 11127−11132.

(72) Wang, L.; Wang, H.-Y.; Gao, B.-R.; Pan, L.-Y.; Jiang, Y.; Chen, Q.-D.; Han, W.; Sun, H.-B. Transient absorption spectroscopic study on band-structure-type change in CdTe/CdS core-shell quantum dots. *IEEE J. Quantum Electron.* **2011**, *47*, 1177−1184.

(73) Peiró, A. M.; Colombo, C.; Doyle, G.; Nelson, J.; Mills, A.; Durrant, J. R. Photochemical reduction of oxygen adsorbed to nanocrystalline TiO$_2$ films: A transient absorption and oxygen scavenging study of different TiO$_2$ preparations. *J. Phys. Chem. B* **2006**, *110*, 23255−23263.

(74) Devahasdin, S.; Fan, C., Jr.; Li, K.; Chen, D. H. TiO$_2$ photocatalytic oxidation of nitric oxide: transient behavior and reaction kinetics. *J. Photochem. Photobiol., A* **2003**, *156*, 161−170.

(75) Tang, J.; Durrant, J. R.; Klug, D. R. Mechanism of photocatalytic water splitting in TiO2. Reaction of water with photoholes, importance of charge carrier dynamics, and evidence for four-hole chemistry. *J. Am. Chem. Soc.* **2008**, *130*, 13885−13891.

(76) Kundu, S.; Kafizas, A.; Hyett, G.; Mills, A.; Darr, J. A.; Parkin, I. P. An investigation into the effect of thickness of titanium dioxide and gold−silver nanoparticle titanium dioxide composite thin-films on photocatalytic activity and photo-induced oxygen production in a sacrificial system. *J. Mater. Chem.* **2011**, *21*, 6854−6863.

(77) Cowan, A. J.; Tang, J.; Leng, W.; Durrant, J. R.; Klug, D. R. Water splitting by nanocrystalline TiO$_2$ in a complete photo-electrochemical cell exhibits efficiencies limited by charge recombination. *J. Phys. Chem. C* **2010**, *114*, 4208−4214.

(78) Raffi, M.; Mehrwan, S.; Bhatti, T. M.; Akhter, J. I.; Hameed, A.; Yawar, W.; ul Hasan, M. M. Investigations into the antibacterial behavior of copper nanoparticles against Escherichia coli. *Ann. Microbiol.* **2010**, *60*, 75−80.

(79) Mattioli, G.; Alippi, P.; Filippone, F.; Caminiti, R.; Amore Bonapasta, A. Deep versus Shallow Behavior of Intrinsic Defects in Rutile and Anatase TiO$_2$ Polymorphs. *J. Phys. Chem. C* **2010**, *114*, 21694−21704.

(80) Deák, P.; Aradi, B.; Frauenheim, T. Polaronic effects in TiO$_2$ calculated by the HSE06 hybrid functional: Dopant passivation by carrier self-trapping. *Phys. Rev. B: Condens. Matter Mater. Phys.* **2011**, *83*, 155207.

(81) Morgan, B. J.; Watson, G. W. Polaronic trapping of electrons and holes by native defects in anatase TiO$_2$. *Phys. Rev. B: Condens. Matter Mater. Phys.* **2009**, *80*, 233102.

(82) Oba, F.; Nishitani, S. R.; Isotani, S.; Adachi, H.; Tanaka, I. Energetics of native defects in ZnO. *J. Appl. Physiol.* **2001**, *90*, 824−828.

(83) Oba, F.; Togo, A.; Tanaka, I.; Paier, J.; Kresse, G. Defect energetics in ZnO: A hybrid Hartree-Fock density functional study. *Phys. Rev. B: Condens. Matter Mater. Phys.* **2008**, *77*, 245202.

(84) Janotti, A.; Van de Walle, C. G. Native point defects in ZnO. *Phys. Rev. B* **2007**, *76*, 165202.

(85) Ágoston, P.; Albe, K.; Nieminen, R. M.; Puska, M. J. Intrinsic n-Type Behavior in Transparent Conducting Oxides: A Comparative Hybrid-Functional Study of In$_2$O$_3$, SnO$_2$ and ZnO. *Phys. Rev. Lett.* **2009**, *103*, 245501.

(86) Scanlon, D. O.; Watson, G. W. On the possibility of p-type SnO$_2$. *J. Mater. Chem.* **2012**, *22*, 25236−25245.

(87) Kılıç, Ç.; Zunger, A. Origins of Coexistence of Conductivity and Transparency in SnO$_2$. *Phys. Rev. B: Condens. Matter Mater. Phys.* **2002**, *88*, 095501.

(88) Singh, A. K.; Janotti, A.; Scheffler, M.; Van de Walle, C. G. Sources of Electrical Conductivity in SnO$_2$. *Phys. Rev. B: Condens. Matter Mater. Phys.* **2008**, *101*, 055502.

(89) Scanlon, D. O. Defect engineering of BaSnO$_3$ for high-performance transparent conducting oxide applications. *Phys. Rev. B: Condens. Matter Mater. Phys.* **2013**, *87*, 161201.

(90) Sallis, S.; Scanlon, D. O.; Chae, S. C.; Quackenbush, N. F.; Fischer, D. A.; Woicik, J. C.; Guo, J.-H.; Cheong, S. W.; Piper, L. F. J. La-doped BaSnO$_3$—Degenerate perovskite transparent conducting oxide: Evidence from synchrotron x-ray spectroscopy. *Appl. Phys. Lett.* **2013**, *103*, 042105.

(91) Deák, P.; Aradi, B.; Frauenheim, T. Quantitative theory of the oxygen vacancy and carrier self-trapping in bulk TiO$_2$. *Phys. Rev. B: Condens. Matter Mater. Phys.* **2012**, *86*, 195206.

(92) Deák, P.; Aradi, B.; Frauenheim, T. Oxygen deficiency in TiO2: Similarities and differences between the Ti self-interstitial and the O vacancy in bulk rutile and anatase. *Phys. Rev. B: Condens. Matter Mater. Phys.* **2015**, *92*, 045204.

(93) Quesada-Gonzalez, M.; Williamson, B. A. D.; Sotelo-Vazquez, C.; Kafizas, A.; Boscher, N. D.; Quesada-Cabrera, R.; Scanlon, D. O.; Carmalt, C. J.; Parkin, I. P. Deeper Understanding of Interstitial

Boron-Doped Anatase Thin Films as A Multifunctional Layer Through Theory and Experiment. *J. Phys. Chem. C* **2018**, *122*, 714−726.

(94) Navas, J.; Sánchez-Coronilla, A.; Aguilar, T.; Hernández, N. C.; de los Santos, D. M.; Sánchez-Márquez, J.; Zorrilla, D.; Fernández-Lorenzo, C.; Alcántara, R.; Martín-Calleja, J. Experimental and theoretical study of the electronic properties of Cu-doped anatase TiO_2. *Phys. Chem. Chem. Phys.* **2014**, *16*, 3835−3845.

(95) Pongwan, P.; Wetchakun, K.; Phanichphant, S.; Wetchakun, N. Enhancement of visible-light photocatalytic activity of Cu-doped TiO_2 nanoparticles. *Res. Chem. Intermed.* **2016**, *42*, 2815−2830.

(96) Yoong, L. S.; Chong, F. K.; Dutta, B. K. Development of copper-doped TiO2 photocatalyst for hydrogen production under visible light. *Energy* **2009**, *34*, 1652−1661.

(97) Shannon, R. D. Revised effective ionic radii and systematic studies of interatomic distances in halides and chalcogenides. *Acta Crystallogr., Sect. A: Found. Crystallogr.* **1976**, *32*, 751−767.

(98) Mathew, S.; Ganguly, P.; Rhatigan, S.; Kumaravel, V.; Byrne, C.; Hinder, S.; Bartlett, J.; Nolan, M.; Pillai, S. Cu-doped TiO_2: visible light assisted photocatalytic antimicrobial activity. *Appl. Sci.* **2018**, *8*, 2067.

(99) Kernazhitsky, L.; Shymanovska, V.; Gavrilko, T.; Naumov, V.; Fedorenko, L.; Kshnyakin, V.; Baran, J. Room temperature photoluminescence of anatase and rutile TiO_2 powders. *J. Lumin.* **2014**, *146*, 199−204.

(100) Varley, J. B.; Janotti, A.; Van de Walle, C. G. Mechanism of visible-light photocatalysis in nitrogen-doped TiO_2. *Adv. Mater.* **2011**, *23*, 2343−2347.

(101) Santara, B.; Giri, P. K.; Imakita, K.; Fujii, M. Evidence for Ti interstitial induced extended visible absorption and near infrared photoluminescence from undoped TiO_2 nanoribbons: an in situ photoluminescence study. *J. Phys. Chem. C* **2013**, *117*, 23402−23411.

(102) Wang, X.; Feng, Z.; Shi, J.; Jia, G.; Shen, S.; Zhou, J.; Li, C. Trap states and carrier dynamics of TiO_2 studied by photoluminescence spectroscopy under weak excitation condition. *Phys. Chem. Chem. Phys.* **2010**, *12*, 7083−7090.

(103) Abazović, N. D.; Čomor, M. I.; Dramićanin, M. D.; Jovanović, D. J.; Ahrenkiel, S. P.; Nedeljković, J. M. Photoluminescence of anatase and rutile TiO_2 particles. *J. Phys. Chem. B* **2006**, *110*, 25366−25370.

(104) Stefan, M.; Pana, O.; Leostean, C.; Bele, C.; Silipas, D.; Senila, M.; Gautron, E. Synthesis and characterization of Fe_3O_4−TiO_2 core-shell nanoparticles. *J. Appl. Phys.* **2014**, *116*, 114312.

(105) Kernazhitsky, L.; Shymanovska, V.; Gavrilko, T.; Naumov, V.; Fedorenko, L.; Kshnyakin, V. Photoluminescence and Optical Absorption of Pure Nanocrystalline TiO_2 Anatase and Rutile at Room Temperature. *J. Nano- Electron. Phys.* **2013**, *5*, 03047-1.

(106) Mathew, S.; kumar Prasad, A.; Benoy, T.; Rakesh, P. P.; Hari, M.; Libish, T. M.; Radhakrishnan, P.; Nampoori, V. P. N.; Vallabhan, C. P. G. UV-visible photoluminescence of TiO_2 nanoparticles prepared by hydrothermal method. *J. Fluoresc.* **2012**, *22*, 1563−1569.

(107) Lyons, J. L.; Alkauskas, A.; Janotti, A.; Van de Walle, C. G. First-principles theory of acceptors in nitride semiconductors. *Phys. Status Solidi B* **2015**, *252*, 900−908.

(108) Frodason, Y.; Johansen, K.; Bjørheim, T.; Svensson, B.; Alkauskas, A. Zn vacancy as a polaronic hole trap in ZnO. *Phys. Rev. B* **2017**, *95*, 094105.